

Adjoint-based assimilation of sparse time-averaged velocity data in large-eddy simulations

Justin Plogmann^{a,b,*}, Oliver Brenner^a, Patrick Jenny^a

^a*Institute of Fluid Dynamics, ETH Zurich, Sonneggstrasse 3, Zürich, CH-8092, Switzerland*

^b*Chemical Energy Carriers and Vehicle Systems Laboratory, Swiss Federal Laboratories for Materials Science and Technology (Empa), Überlandstrasse 129, Dübendorf, CH-8600, Switzerland*

Abstract

The need for accurate and fast scale-resolving simulations of fluid flows, where turbulent dispersion is a crucial physical feature, is evident. Large-eddy simulations (LES) are computationally more affordable than direct numerical simulations, but their accuracy depends on sub-grid scale models and the quality of the computational mesh. In order to compensate related errors, a data assimilation approach for LES is devised in this work.

The presented method is based on variational assimilation of sparse time-averaged velocity reference data through a stationary corrective forcing term in the LES momentum equation working with the time-averaged LES momentum equation allows to employ a stationary discrete adjoint method. Therefore, the stationary forcing in the unsteady LES momentum equation is iteratively updated within the gradient-based optimization framework in conjunction with the adjoint gradient. The implementation is based on a three-dimensional LES solver in *OpenFOAM*, which is extended to allow the computation of adjoint quantities and, ultimately, the adjoint gradient.

Efficacy of the proposed framework is demonstrated for turbulent flow over periodic hills and around a square cylinder. Coarse meshes are leveraged to further enhance the speed of the optimization procedure. Time- and spanwise-averaged velocity reference data from high-fidelity simulations is taken from the literature.

Our results demonstrate that adjoint-based assimilation of averaged velocity enables the optimization of the mean flow, vortex shedding frequency (i. e., Strouhal number), and turbulent kinetic energy. This highlights the superiority of scale-resolving simulations such as LES over simulations based on the (unsteady) Reynolds-averaged equations.

Keywords: Data assimilation, LES, Unsteady, Sparse data, Discrete adjoint, OpenFOAM

1. Introduction

The simulation of turbulent flows remains one of the major challenges in computational fluid dynamics (CFD). Direct numerical simulations (DNS) of complex flow problems at high Reynolds numbers are still unfeasible since the computational cost scales with Re^3 . In turn, the accuracy of simulations based on the Reynolds-averaged Navier–Stokes (RANS) equations relies on model assumptions. Since all turbulent scales are modeled and none of the turbulence is resolved, the accuracy of RANS simulations highly depends on the choice of the turbulence model and the model parameters. For this reason, dissipation is often over-predicted in RANS simulations [1]. The same applies to unsteady RANS (URANS) simulations [2]. Nevertheless, RANS models are most commonly used for industrial flows, as their computational cost is low, but they are less suitable for flows where turbulent diffusion is important, e. g., in combustion, where species dispersion is crucial (e. g., in exhaust plumes in the wake of a vehicle [3, 4] or pollutant dispersion in urban flows [5]).

With increasing computational resources, large-eddy simulations (LES) are being used more and more in these areas. LES involve solving the spatially filtered Navier–Stokes equations while the objective is to resolve the large turbulent structures and to model the effect of the small ones. Since only the smaller structures are directly subjected to modeling errors, LES provides a favorable compromise, particularly for free shear flows, as the computational expense is only moderately influenced by the Reynolds number (approximately proportional to $Re^{0.4}$) [6, 7]. When it comes to wall-resolved LES, however, the computational cost scales approximately with $Re^{1.8}$ [8, 9]. Due to the high cost of LES for applications with wall turbulence, hybrid LES/RANS methods have received considerable attention [10]. There, LES is typically supported by RANS simulations in regions where the LES is under-resolved (e. g., [11, 12]).

*Corresponding author: justin.plogmann@empa.ch

In this work, however, we aim to enhance LES by data assimilation (DA) in order to reduce errors that are introduced by, e.g., the turbulence model or a coarse computational mesh [13, 14]. In general, there exist two main approaches in DA. In statistical DA, e.g., based on the ensemble Kalman filter (EnKF) [15], observations are incorporated into the model one at a time as they become available. This approach sequentially updates the model’s state estimate based on the current observations. For instance, in weather forecasting, sequential DA allows for continuous integration of observations from satellites, weather stations, and other sources to improve short-term predictions. Variational DA, on the other hand, formulates the assimilation problem as an optimization task, seeking the best model state that fits both the observations and the model dynamics. It involves minimizing a cost function that measures the misfit between model predictions and observations subject to constraints and regularization terms [16, 17].

DA can also be categorized into stationary and dynamic [16]. Dynamic DA approaches like the EnKF or four-dimensional variational (4DVar) DA incur huge computational costs since the flow dynamics cannot be neglected over a time interval during which observations are assimilated. EnKF have been extensively applied in the context of meteorology, and more recently also in the field of fluid mechanics [18, 19]. Different attempts to reduce the computational cost of 4DVar DA for turbulent flows were also made (cf. [20, 21, 22]). This allowed to assimilate time-resolved data in LES, but the computational cost associated with these dynamic DA approaches is still very high, and time-resolved data is required.

Recent works have applied stationary DA to optimize simulations of steady-state flows using sparse data by performing three-dimensional variational (3DVar) DA, enabling the reconstruction of mean flow at a low computational cost (e.g., [23, 24, 25, 26, 27, 28, 29, 30, 31]). An extension of 3DVar DA for unsteady flows was presented in Plogmann et al. [32]. There, time-averaging the URANS momentum equation was introduced to construct a stationary adjoint equation so that sparse time-averaged velocity reference data could ultimately be assimilated. This allowed to optimize a stationary corrective forcing term in the (unsteady) URANS momentum equation, which allowed for mean flow reconstruction and an improved vortex shedding frequency of different turbulent wake flows at a low computational cost. An extension of their method was presented in [33] for flows with time-periodic statistics. Central to the proposed methodology is introducing a corrective, divergence-free, and unsteady forcing term derived from a Fourier series expansion into the unsteady momentum equations. This term allows the tuning of stationary parameters across different Fourier modes, whereby the flow dynamics could be further improved.

In the present study, we aim to assimilate sparse time-averaged velocity reference data (obtained from high-fidelity LES and DNS) into coarse LES. Therefore, the framework from [32] is adapted, but LES serve as the forward problem instead of URANS simulations. We investigate turbulent flows over a periodic hill at a Reynolds number of 10595 and around a square cylinder at a Reynolds number of 22000. Notably, after optimization, mean flow and turbulent kinetic energy (TKE) are in better agreement with the reference.

To the best of our knowledge, this is the first work demonstrating the variational assimilation of sparse time-averaged velocity reference data into LES. Furthermore, our DA framework comes with multiple advantages. Only time-averaged data is required, even though the simulations are unsteady. Additionally, the cost of the employed 3DVar DA scheme is relatively low due to our efficient semi-analytical approach for the computation of the cost function gradient within the discrete adjoint method.

The remainder of the paper is organized as follows. The method is introduced in section 2, and the results of data assimilation applied to two different flow configurations are discussed in section 3. Finally, in section 4, the work is summarized, and future developments are suggested.

2. Methods

2.1. Problem statement

2.1.1. Filtered Navier–Stokes equations

In the following, the turbulent flow of an incompressible Newtonian fluid is considered. Applying a low-pass filter to the Navier–Stokes equations yields the governing equations for LES. Thus, any instantaneous field ξ is split into a filtered part $\bar{\xi}$ and a residual part ξ' . The LES governing equations are written as

$$\frac{\partial \bar{u}_j}{\partial x_j} = 0 \tag{1}$$

and

$$\frac{\partial \bar{u}_i}{\partial t} + \frac{\partial \bar{u}_i \bar{u}_j}{\partial x_j} + \frac{\partial}{\partial x_i} \left[\frac{\bar{p}}{\rho} \right] - \frac{\partial}{\partial x_j} [2\nu \bar{S}_{ij}] + \frac{\partial \tau_{ij}^r}{\partial x_j} = 0 \tag{2}$$

with $\rho = \text{const.}$ and the filtered rate-of-strain tensor

$$\bar{S}_{ij} = \frac{1}{2} \left(\frac{\partial \bar{u}_i}{\partial x_j} + \frac{\partial \bar{u}_j}{\partial x_i} \right). \quad (3)$$

The residual stresses

$$\tau_{ij}^r = \overline{u_i u_j} - \bar{u}_i \bar{u}_j, \quad (4)$$

are modeled using the Boussinesq hypothesis, i. e.,

$$\tau_{ij}^r = \frac{2}{3} k_{\text{sgs}} \delta_{ij} - 2\nu_{\text{sgs}} \bar{S}_{ij} \quad (5)$$

with the sub-grid scale (SGS) viscosity ν_{sgs} and the isotropic part of the residual stress tensor, where the SGS TKE is defined as

$$k_{\text{sgs}} = \frac{1}{2} \tau_{ii}^r. \quad (6)$$

2.1.2. Data assimilation parameter

To account for discrepancies in the divergence of the residual stresses, we introduce a corrective force f_i such that

$$\frac{\partial \tau_{ij}^r}{\partial x_j} = \frac{\partial}{\partial x_j} \left(\frac{2}{3} k_{\text{sgs}} \delta_{ij} - 2\nu_{\text{sgs}} \bar{S}_{ij} \right) - f_i, \quad (7)$$

which is then subjected to a Stokes–Helmholtz decomposition, similarly done in [23, 34, 26, 27], i. e.,

$$f_i = -\frac{\partial \phi}{\partial x_i} + \epsilon_{ijk} \frac{\partial \psi_k}{\partial x_j}, \quad (8)$$

with the scalar potential ϕ , the vector potential ψ , and the Levi-Civita symbol ϵ_{ijk} .

For the modeled LES momentum equation this yields

$$\frac{\partial \bar{u}_i}{\partial t} + \frac{\partial \bar{u}_i \bar{u}_j}{\partial x_j} + \frac{\partial p^*}{\partial x_i} - \frac{\partial}{\partial x_j} [2\nu_{\text{eff}} \bar{S}_{ij}] - \epsilon_{ijk} \frac{\partial \psi_k}{\partial x_j} = 0 \quad (9)$$

with the effective viscosity

$$\nu_{\text{eff}} = \nu + \nu_{\text{sgs}}, \quad (10)$$

and where the filtered pressure \bar{p} , the residual TKE k_{sgs} , and the scalar potential ϕ are absorbed into the modified pressure as

$$p^* = \frac{\bar{p}}{\rho} + \frac{2}{3} k_{\text{sgs}} + \phi. \quad (11)$$

Out of convenience, the modified pressure p^* is denoted as \bar{p} from now on. The data assimilation acts directly on ψ_k ; that is, no additional equations need to be solved for ϕ and ψ_k .

2.1.3. Temporal averaging of the LES equations

To leverage the discrete adjoint method for stationary flows from [25] and apply it to unsteady flow problems, temporal averaging is introduced. Therefore, a filtered quantity $\bar{\xi}$ is split into a temporal average $\langle \cdot \rangle$ and corresponding fluctuation $(\cdot)''$ as

$$\bar{\xi} = \langle \bar{\xi} \rangle + \bar{\xi}'' . \quad (12)$$

A detailed derivation of time-averaging the momentum equation is given in [32]. With all terms expanded and rearranged, we obtain

$$R_{\langle \bar{u}_i \rangle} = \frac{\partial \langle \bar{u}_i \rangle \langle \bar{u}_j \rangle}{\partial x_j} + \frac{\partial \langle \bar{p} \rangle}{\partial x_i} - \frac{\partial}{\partial x_j} (2(\nu + \langle \nu_{\text{sgs}} \rangle) \langle \bar{S}_{ij} \rangle) - \underbrace{\frac{\partial}{\partial x_j} (2 \langle \nu_{\text{sgs}}'' \bar{S}_{ij}'' \rangle)}_{\text{additional stress terms}} + \frac{\partial \langle \bar{u}_i'' \bar{u}_j'' \rangle}{\partial x_j} - \epsilon_{ijk} \frac{\partial \psi_k}{\partial x_j} = 0 \quad (13)$$

for the LES momentum equation residual.

The structure of eq. (13) is very similar to the modeled LES momentum equation (9), except that it describes a stationary state and that it features two additional terms due to the time-averaging process, which are treated

explicitly in the adjoint problem discretization. The discrete adjoint method is now applied to the time-averaged LES equations (13).

To ensure converged averaged properties of the flow fields, which are needed in conjunction with their corresponding fluctuations to construct eq. (13), we introduce a global measure C_U for the change in an averaged field (cf. eq. (A.1)). The criterion is set such that the averaged quantities converge well, but the number of time steps needed in the forward solution is kept as small as possible to minimize the required CPU time. Therefore, the criterion is case-dependent and is set individually for each case as discussed in section 3.

2.2. Forward problem formulation

The forward problem solution consists of solving the momentum equation for \bar{u}_i and the pressure equation for \bar{p} . Hence, the forward problem solution vector, which is time-dependent, is defined as

$$\begin{bmatrix} \bar{u} \\ \bar{p} \end{bmatrix} = \begin{bmatrix} \bar{u}_x \\ \bar{u}_y \\ \bar{u}_z \\ \bar{p} \end{bmatrix}, \quad (14)$$

which is obtained via the PISO algorithm discussed in section 2.7. Note that \bar{u}_x , \bar{u}_y , \bar{u}_z , and \bar{p} are vectors of length n , where n is the number of grid cells.

2.3. Time-averaged forward problem formulation

While solving the forward problem, time-averaging is performed to obtain $\langle \bar{u} \rangle$, $\langle \bar{p} \rangle$, $\langle \nu_{sgs} \rangle$, and the additional terms in eq. (13). The time-averaged forward system of equations is linearized in a *coupled* manner as

$$R(\psi, U) = \begin{bmatrix} R_{\langle \bar{u} \rangle}(\psi, U) \\ R_{\langle \bar{p} \rangle}(\psi, U) \end{bmatrix} = \begin{bmatrix} \mathbf{A}_{\langle \bar{u} \rangle \langle \bar{u} \rangle} & \mathbf{A}_{\langle \bar{u} \rangle \langle \bar{p} \rangle} \\ \mathbf{A}_{\langle \bar{p} \rangle \langle \bar{u} \rangle} & \mathbf{A}_{\langle \bar{p} \rangle \langle \bar{p} \rangle} \end{bmatrix} \begin{bmatrix} \langle \bar{u} \rangle \\ \langle \bar{p} \rangle \end{bmatrix} - \begin{bmatrix} b_{\langle \bar{u} \rangle} \\ b_{\langle \bar{p} \rangle} \end{bmatrix} = \mathbf{A}_U U - b_U = 0, \quad (15)$$

where ψ represents the parameter used for data assimilation and

$$U = \begin{bmatrix} \langle \bar{u} \rangle \\ \langle \bar{p} \rangle \end{bmatrix} = \begin{bmatrix} \langle \bar{u}_x \rangle \\ \langle \bar{u}_y \rangle \\ \langle \bar{u}_z \rangle \\ \langle \bar{p} \rangle \end{bmatrix}; \quad (16)$$

again, $\langle \bar{u}_x \rangle$, $\langle \bar{u}_y \rangle$, $\langle \bar{u}_z \rangle$, and $\langle \bar{p} \rangle$ are vectors of length n . The system matrix \mathbf{A}_U of the *coupled* linear system of time-averaged equations is composed of sub-matrices that describe the implicit contributions.

2.4. Inverse problem formulation

To measure the misfit between the LES model output and the existing reference data, the scalar cost functional f is introduced. It consists of a regularization function f_ψ and a discrepancy contribution f_U , i. e.,

$$f(\psi, U) = f_\psi(\psi) + f_U(U), \quad (17)$$

and the optimization problem

$$\min_{\psi} f(\psi, U) \quad (18a)$$

$$\text{subject to } R(\psi, U) = 0 \quad (18b)$$

describes the data assimilation procedure, where ψ is the parameter to be iteratively optimized and U is the time-averaged forward problem solution. Due to the nonlinearity, a non-linear optimization solver is used, but without regularization, there is no assurance that the solution is unique [23]. Therefore, regularization is introduced to reduce the ambiguity (see sec. 2.4.2).

2.4.1. Discrete adjoint method

The cost function gradient is derived by defining a Lagrangian

$$\mathcal{L}(\psi, U) = f(\psi, U) - \lambda^T R(\psi, U) \quad (19)$$

with the spatially varying Lagrange multipliers

$$\lambda = \begin{bmatrix} \lambda_{\langle \bar{u} \rangle} \\ \lambda_{\langle \bar{p} \rangle} \end{bmatrix} = \begin{bmatrix} \lambda_{\langle \bar{u}_x \rangle} \\ \lambda_{\langle \bar{u}_y \rangle} \\ \lambda_{\langle \bar{u}_z \rangle} \\ \lambda_{\langle \bar{p} \rangle} \end{bmatrix}, \quad (20)$$

where $\lambda_{\langle \bar{u}_x \rangle}$, $\lambda_{\langle \bar{u}_y \rangle}$, $\lambda_{\langle \bar{u}_z \rangle}$, and $\lambda_{\langle \bar{p} \rangle}$ are vectors of length n . The cost function gradient with respect to the parameters ψ is derived as

$$\frac{df}{d\psi} = \frac{\partial f_\psi}{\partial \psi} - \lambda^T \frac{\partial R}{\partial \psi}, \quad (21)$$

and following Brenner et al. [24], λ is obtained by solving the adjoint equation

$$\left(\frac{\partial R}{\partial U} \right)^T \lambda \approx \mathbf{A}_U^T \lambda = \frac{\partial f_U}{\partial U}^T, \quad (22)$$

where the right-hand side is analytically derived from the cost function and thus comes at low computational cost. The cost of solving this system for λ is negligible compared to that for solving the forward problem, and it is independent of the number of parameters $\psi_k (3n)$.

Applied to the time-averaged LES forward problem with residual eq. (13) and cost function f_U , the *coupled* adjoint system of equations (22), reads

$$\begin{bmatrix} \mathbf{A}_{\langle \bar{u} \rangle \langle \bar{u} \rangle}^T & \mathbf{A}_{\langle \bar{p} \rangle \langle \bar{u} \rangle}^T \\ \mathbf{A}_{\langle \bar{u} \rangle \langle \bar{p} \rangle}^T & \mathbf{A}_{\langle \bar{p} \rangle \langle \bar{p} \rangle}^T \end{bmatrix} \begin{bmatrix} \lambda_{\langle \bar{u} \rangle} \\ \lambda_{\langle \bar{p} \rangle} \end{bmatrix} = \begin{bmatrix} \frac{\partial f_{\langle \bar{u} \rangle}}{\partial \langle \bar{u} \rangle}^T \\ \frac{\partial f_{\langle \bar{p} \rangle}}{\partial \langle \bar{p} \rangle}^T \end{bmatrix}. \quad (23)$$

For the evaluation of the adjoint gradient in eq. (21), the derivative of R with respect to parameter ψ is needed. Thus, the forward problem R is numerically linearized with respect to parameter ψ in *OpenFOAM* as

$$R = \mathbf{A}_\psi \psi - b_\psi = 0, \quad (24)$$

such that the derivative of R with respect to parameter ψ reads

$$\frac{\partial R}{\partial \psi} = \frac{\partial}{\partial \psi} [\mathbf{A}_\psi \psi - b_\psi] = \mathbf{A}_\psi. \quad (25)$$

Solving eq. (22) for λ using eq. (25) results in

$$\frac{df}{d\psi} = \frac{\partial f_\psi}{\partial \psi} - \lambda_{\langle \bar{u}_x \rangle}^T \mathbf{A}_{\langle \bar{u}_x \rangle, \psi} - \lambda_{\langle \bar{u}_y \rangle}^T \mathbf{A}_{\langle \bar{u}_y \rangle, \psi} - \underbrace{\lambda_{\langle \bar{u}_z \rangle}^T \mathbf{A}_{\langle \bar{u}_z \rangle, \psi}}_{= 0 \text{ if 2D}} - \underbrace{\lambda_{\langle \bar{p} \rangle}^T \mathbf{A}_{\langle \bar{p} \rangle, \psi}}_{= 0} \quad (26)$$

for the discrete adjoint gradient. Due to the divergence-free property of the forcing term, there is no contribution of parameter ψ_k to the pressure equation. The derivative of the pressure residual with respect to the parameter is thus zero, and there is no contribution of the adjoint pressure $\lambda_{\langle \bar{p} \rangle}$ to the adjoint gradient.

2.4.2. Cost function and regularization

The discrepancy part of the cost function measures agreement of the time-averaged forward problem solution U with the reference data U^{ref} . In the presented application, only time- and spanwise-averaged velocity data is assimilated, i. e.,

$$f_U(U) = \sum_{j \in \mathcal{R}} \left[\sum_{k \in \{x, y, z\}} (\langle \bar{u}_{k,j} \rangle - \langle \bar{u}_{k,j}^{\text{ref}} \rangle)^2 \right], \quad (27)$$

where \mathcal{R} is the list of reference cell indices j . L_2 regularization is chosen to reduce the ambiguity of the inverse problem. Therefore, regularization is applied to the (divergence-free) corrective forcing term. The reason for this approach is that the forcing term is introduced to correct the mean flow but not the fluctuations of the velocity. In terms of time-averaged velocity, the initial LES is supposed to give adequate results relatively close to the time-averaged velocity reference data. It is, therefore, in order to avoid the suppression or damping of velocity fluctuations, that only a minimal correction is sought.

Hence, a function of the form

$$f_\psi(\psi) = C^{\text{reg}} \|\nabla \times \psi\|_2^2 \quad (28)$$

with hyperparameter C^{reg} is used to punish strong peaks in the corrective forcing term field. An appropriate hyperparameter is found when cost and test functions (see sec. 2.4.3) decrease during optimization.

2.4.3. Test function

In addition, we introduce the test function

$$f^{\text{test}} = \frac{1}{V^{\text{test}}} \sum_{j \in \mathcal{T}} \left[\sum_{k \in \{x,y,z\}} (\langle \bar{u}_{k,j} \rangle - \langle \bar{u}_{k,j}^{\text{ref}} \rangle)^2 V_j \right], \quad (29)$$

where \mathcal{T} is the list of test cell indices j , V_j the volume of cell j , and V^{test} the total volume of all test cells. The test data points are all remaining points in the domain that are not defined as reference points. This concept is often considered in machine learning, where training, validation, and test data are considered.

2.5. Optimization

The gradient-based fixed step size optimization algorithm is employed to perform updates of optimization parameter ψ from iteration step (n) to ($n + 1$) as

$$\psi_i^{(n+1)} = \psi_i^{(n)} - \eta \frac{df^{(n)}}{d\psi_i} \quad (30)$$

with the fixed step size η , which is case dependent.

2.6. Reference data

Data assimilation was performed using public online reference data from the literature [35, 36], in particular, spanwise and temporally averaged LES or DNS velocity data.

The *SciPy* library in *Python* offers the *griddata* interpolation function, which is utilized for unstructured data interpolation on *OpenFOAM* meshes to map reference data onto cell center locations. Specifically, the nearest neighbor method is utilized for this interpolation. To differentiate between reference and test data sets within these fields, two indicator fields are introduced, marking cells designated for testing and reference purposes, respectively.

2.7. Implementation

The versions *OpenFOAM-v1912* [37] and *foam-extend-5.0* [38] of the open-source field operation and manipulation platform, *OpenFOAM*, known for its computational fluid dynamics (CFD) solvers, are utilized for the forward and adjoint problems, respectively, leveraging the platform's pre-existing solvers and diverse capabilities. The approach adopted for solving the forward problem involves the PISO algorithm, and a fully *coupled* solution process is chosen for the adjoint problem. Notably, the *pisoFoam* and *transientFoam* solvers were extended, respectively.

The computational meshes were created using *blockMesh*, and the cell size is decreasing toward the solid walls to capture certain flow features well enough. However, the resolution in the wall-normal direction was still chosen quite coarse in order to allow for larger time steps, which in turn drastically decreases the CPU time of the forward simulation. This methodology of mesh generation was applied to all cases in this work.

Second-order schemes are used for spatial and temporal discretizations. The time step sizes for all cases ensure a maximum Courant-Friedrichs-Lewy (CFL) number smaller than one. For this work, the one-equation SGS TKE model as proposed by Yoshizawa and Horiuti [39] was used. For the forward problem, a conjugate gradient linear solver with a DIC preconditioner was used for the pressure, whereas the discretized SGS TKE was solved by a bi-conjugate gradient stabilized linear solver with a DILU preconditioner. The bi-conjugate gradient stabilized linear solver without preconditioning was applied to solve the *coupled* adjoint system. Parallel computing was used for the forward simulation but not for the adjoint problem solution. The optimization itself was performed in *Python* using *PyFoam* to interact with the *OpenFOAM* solvers.

The DA procedure is depicted in fig. 1. First, the forward problem (3D LES) is solved to obtain the forward solution U as a function of the parameter field ψ . Meanwhile, time-averaging of the LES solution is performed, and the solver stops as soon as the averages converge according to eq. (A.1). Since only quasi-two-dimensional flows are considered in this work, spanwise-averaging is introduced, such that the averaged quantities are mapped on a corresponding two-dimensional mesh. Then, the time- and spanwise-averaged and converged forward system matrix $\frac{\partial R}{\partial U}$ is used in conjunction with the analytical evaluation of the right-hand side of eq. (22) to solve the two-dimensional adjoint

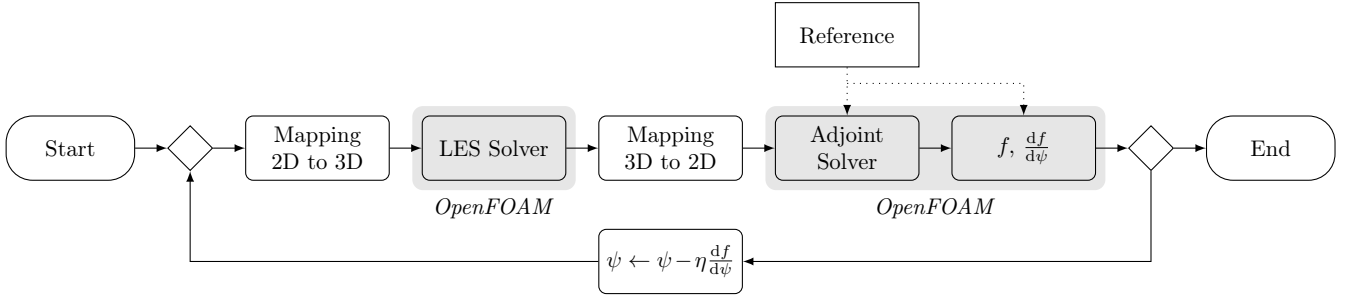


Figure 1: Flowchart of the optimization-based data assimilation procedure.

system for the Lagrange multipliers λ . Third, the matrix $\frac{\partial R}{\partial \psi}$ is constructed and, together with the regularization function and the Lagrange multipliers λ , used to compute the adjoint gradient. The current parameter values and the corresponding gradient are then used in the optimization step to update the parameter field, which is mapped back onto the three-dimensional mesh.

3. Results and discussion

In this section, the results of the proposed data assimilation approach are presented for flows over periodic hills and around a square cylinder.

3.1. Flow over periodic hills

The periodic hill geometry is depicted in fig. 2. Velocity data from highly resolved LES by Gloerfelt and Cinnella [35], averaged in time and in z -direction, is considered as reference. This setup features a flow at a Reynolds number of

$$\text{Re} = \frac{\bar{u}_b H}{\nu} = 10\,595 \quad (31)$$

based on the bulk velocity \bar{u}_b over the hill crest of height H and the kinematic viscosity ν .

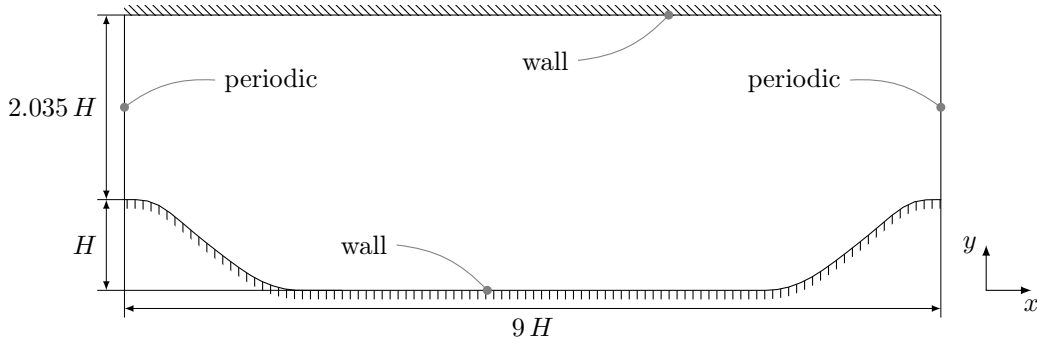


Figure 2: Simulation domain of the periodic hill setup. The mean flow is in x -direction. All length scales are normalized by the hill crest height H . The domain extends over a width of $4.5H$ in z -direction, in which periodicity is assumed.

At the upper and lower walls no-slip condition is set for the velocity and Neumann condition for the pressure and the SGS viscosity. The SGS TKE is set to zero at the upper and lower walls.

Due to the quasi-two-dimensional flow setup (infinitely long hills in spanwise direction), a mapping onto a two-dimensional mesh with the same resolution in the xy -plane (but only one cell in z -direction) is introduced. Therefore, averaging is not only performed in time, but also in spanwise direction.

3.1.1. Optimization using a coarse mesh

The forward problem is solved on two different meshes. First, a coarse mesh with 74 cells in x -direction by 37 cells in y -direction by 36 cells in z -direction (total cell count is 98 568) is used. This mesh is too coarse for proper LES, particularly in near-wall regions, but the cell aspect ratio is quite low everywhere.

In fig. 3a, an instantaneous snapshot of the streamwise velocity component is depicted, which is taken during the run-time of the initial LES. Since the mesh is very coarse, small-scale motions are not resolved, but larger structures

are clearly visible. Fig. 3b illustrates the time- and spanwise-averaged streamwise velocity component of the initial LES. As discussed in sec. 2.1.3, the averaged quantities (here only velocity is shown) serve for the construction of the stationary adjoint equation (13). Therefore, the averaging criterion (cf. eq. (A.1)) needs to be set appropriately to ensure well-converged quantities such that the adjoint problem can be considered stationary.

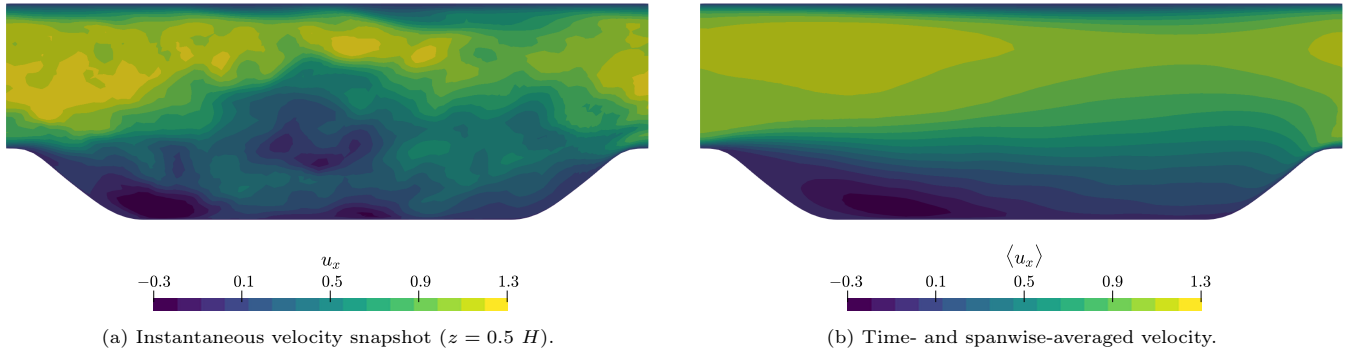


Figure 3: Streamwise velocity component of the flow over periodic hills. The LES solver ran until the convergence criterion $C_U = 0.15$ was reached.

For the optimization, reference points must be selected where averaged velocity data is assimilated. As quite extensively discussed in Brenner et al. [25] and Plogmann et al. [32], the optimal placement of such reference data points is crucial and has a strong influence on the quality of mean flow reconstruction. Furthermore, the number of reference data points should ideally be as small as possible, as in practical applications, it represents the number of (e. g., pointwise) measurements. The focus of this work, however, is to demonstrate that with a sufficient number of reference data points, the mean flow can be well predicted using such coarse LES.

In fig. 4a, the reference data point distribution is shown. The density of points increases toward the walls, and an almost uniform spacing is chosen for the x -direction. The cost function, depicted in fig. 4c, decreases during optimization; the discrepancy part decreases roughly by two orders of magnitude, while the test function reduces by one order of magnitude. Hence, the optimization works effectively throughout the entire domain. Moreover, the regularization ensures physically meaningful velocity profiles (cf. fig. 4b). It is evident that the average velocity from the initial LES drastically deviates from the average reference velocity due to the poor resolution. Especially velocity gradients near the wall are not well captured and thus deteriorate the overall mean flow solution. The averaged velocity profiles after optimization match the reference well, apart from some peaks near the upper wall. There, the mesh resolution is particularly coarse, such that the corrective force cannot account for the drastic change of the velocity profiles in this region.

Since the mean velocity gradients near the upper wall are larger after optimization, the sub-grid scale model compensates for this effect with a larger contribution to the sub-grid scale viscosity and, hence, also to the sub-grid scale TKE. Therefore, the total TKE profiles show a big deviation close to the upper wall, while major improvements are made downstream of the recirculation zone. The TKE within the recirculation zone, however, does not match the reference better after optimization. One reason is the too-coarse mesh, and another is the chosen sub-grid scale model. Especially downstream of the hill, where mean shear rates are high, and separation occurs, the mesh resolution is insufficient, and the reference data point placement could be optimized.

To this end, we would like to mention that TKE data or other higher-order moments have not been assimilated. Rather, the divergence of the average residual stresses is corrected, which ultimately allows for mean flow reconstruction in conjunction with improved turbulent quantities.

3.1.2. Optimization using a coarse mesh with increased wall-normal resolution

Now, another mesh with 74 cells in x -direction by 60 cells in y -direction by 36 cells in z -direction (total cell count is 159 840) is introduced. In general, this mesh is also coarse for LES, but it features a higher resolution in the wall-normal directions. Therefore, the cell aspect ratio increases toward the walls and results in a more anisotropic mesh compared to the one from sec. 3.1.1.

For this mesh configuration, a similar reference data point distribution as the one used with the coarse mesh has been adopted (cf. fig. 5a). Depicted in fig. 5c and as observed before, the discrepancy part of the cost function decreases by approximately two orders of magnitude alongside a significant reduction of the test function due to regularization. Overall, the averaged, optimized velocity profiles shown in fig. 5b match very well with the reference. The higher wall-normal resolution allows for smoother averaged velocity profiles. Especially close to the upper wall, non-physical

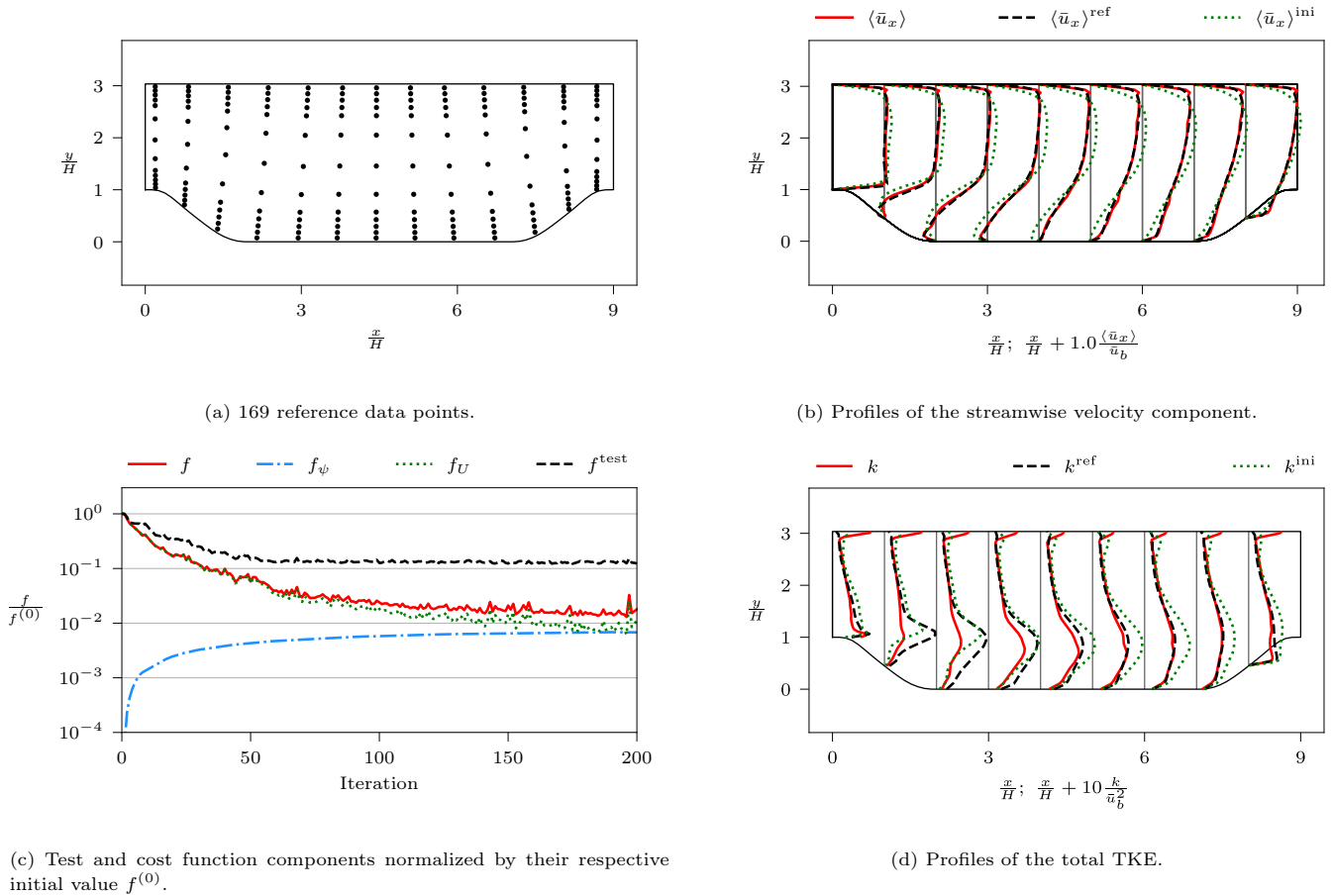


Figure 4: Optimization of the time- and spanwise-averaged flow over periodic hills using a coarse mesh. Optimization step size is $\eta = 7 \times 10^{-2}$ with a maximum number of optimization steps $N_{\text{opt}} = 200$. The forward problem solver ran until the convergence criterion $C_U = 0.15$ was reached, and the regularization weight parameter was set to $C^{\text{reg}} = 1 \times 10^{-5}$.

peaks in the mean velocity profiles are no longer present. Moreover, the initial deviation from the reference profiles is smaller on this mesh (compare figs. 4b and 5b). Therefore, the forcing term does not need to correct as much and thus is less intrusive, which also allows for a smaller regularization weight. Additionally, the increased resolution toward the upper wall promotes more accurate TKE profiles in the upper wall vicinity. The mean velocity gradients are better captured, and hence, the optimized TKE profiles improved in comparison to the case with lower wall-normal resolution. Nevertheless, the TKE profiles in the remaining part of the domain are similar for the two different meshes since the mesh resolution in x -direction and z -direction, and away from the walls also in y -direction, are the same. Consequently, the computational meshes are too coarse to dynamically resolve the TKE in the recirculation zone. In this work, however, the aim is to demonstrate the basic capabilities of the proposed framework rather than assessing its resolution limits.

3.2. Flow around square cylinder

Next, we consider the flow around a square cylinder. The forward problem is solved on a coarse (not near-wall resolving) mesh with a total of 139 400 cells. The two-dimensional mesh (for the adjoint problem) with the same resolution in the x - y -plane and therefore consists of 6970 cells. A sketch of the geometry and boundaries is provided in fig. 6. All length scales are expressed relative to the cylinder width D , which also serves as the length scale to compute the Reynolds number. The flow is analyzed for

$$\text{Re} = \frac{\bar{u}_\infty D}{\nu} = 22\,000,$$

where \bar{u}_∞ is the free-stream velocity. Averaged DNS data taken from [36] provides the reference.

Boundary conditions for velocity and pressure are also taken from [36]. For the SGS viscosity, Neumann conditions are applied at all boundaries. At the inlet and the cylinder wall, Dirichlet condition is applied and set to a very small

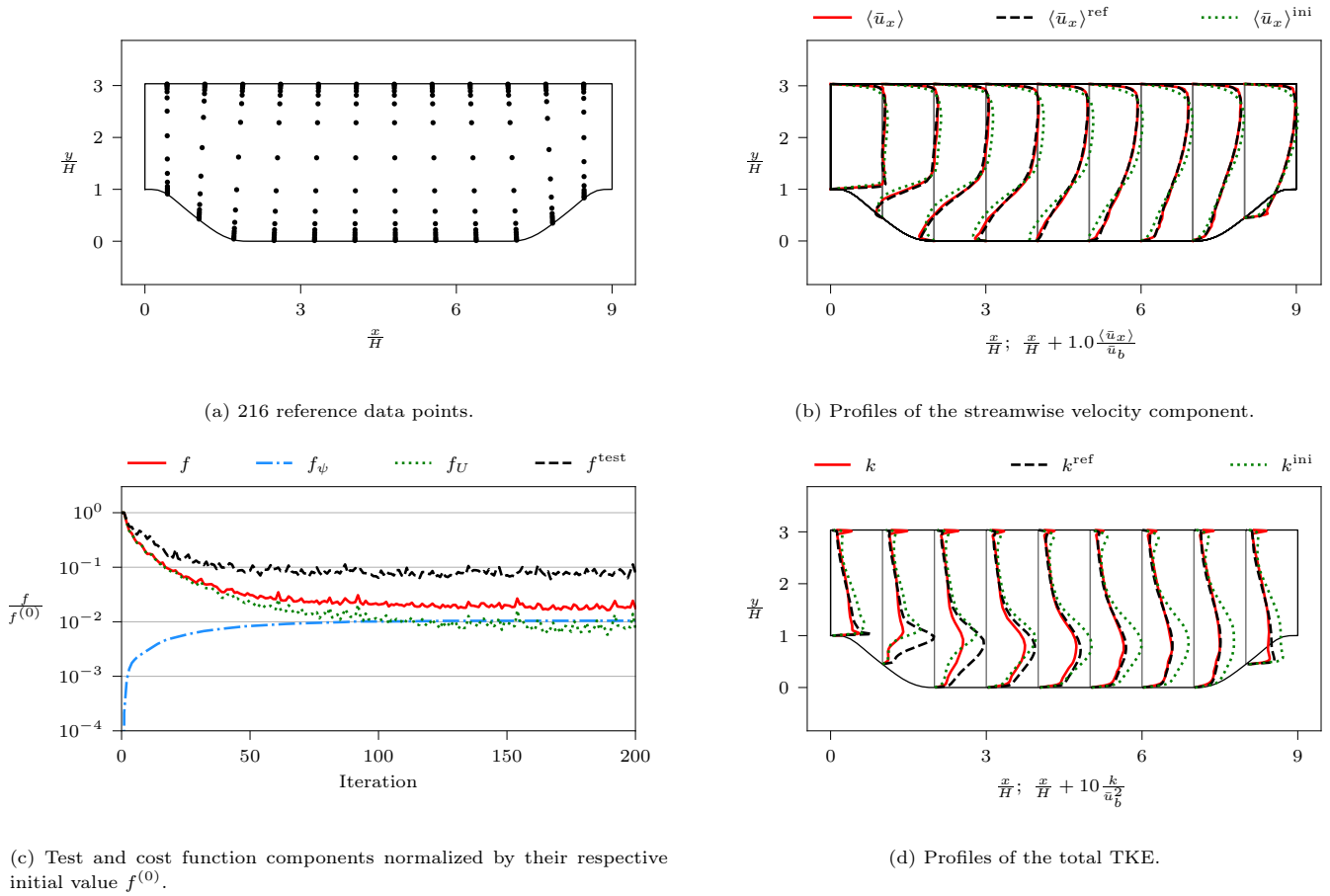


Figure 5: Optimization of the time- and spanwise-averaged flow over periodic hills using a coarse mesh with increased wall-normal resolution. Optimization step size is $\eta = 9 \times 10^{-2}$ with a maximum number of optimization steps $N_{\text{opt}} = 200$. The forward problem solver ran until the convergence criterion $C_U = 0.15$ was reached, and the regularization weight parameter was set to $C^{\text{reg}} = 5 \times 10^{-7}$.

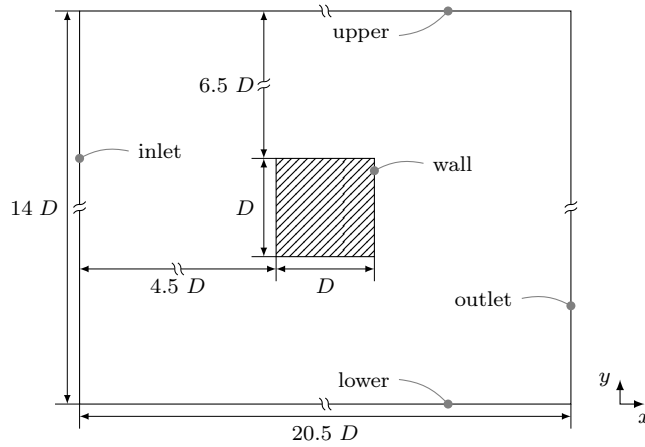


Figure 6: Simulation domain of the square cylinder setup with mean flow in x -direction. All length scales are normalized by cylinder width D , and the domain features a depth of $9.8 D$ in z -direction with periodic boundary conditions.

value for the SGS TKE (according to [36]), and Neumann conditions are set at the outlet as well as the upper and lower boundaries.

3.2.1. Optimization

As visualized in fig. 7a, most of the selected reference data points are accumulated around the cylinder with additional ones along the y -direction in the near-wake regions. Regarding the optimization, the discrepancy part of the cost function decreases by roughly one order of magnitude, as shown in fig. 7c. Moreover, the test function was only reduced by a factor of two to three. Again, we would like to mention that test data points are located in every grid cell that was not used as a source for DA.

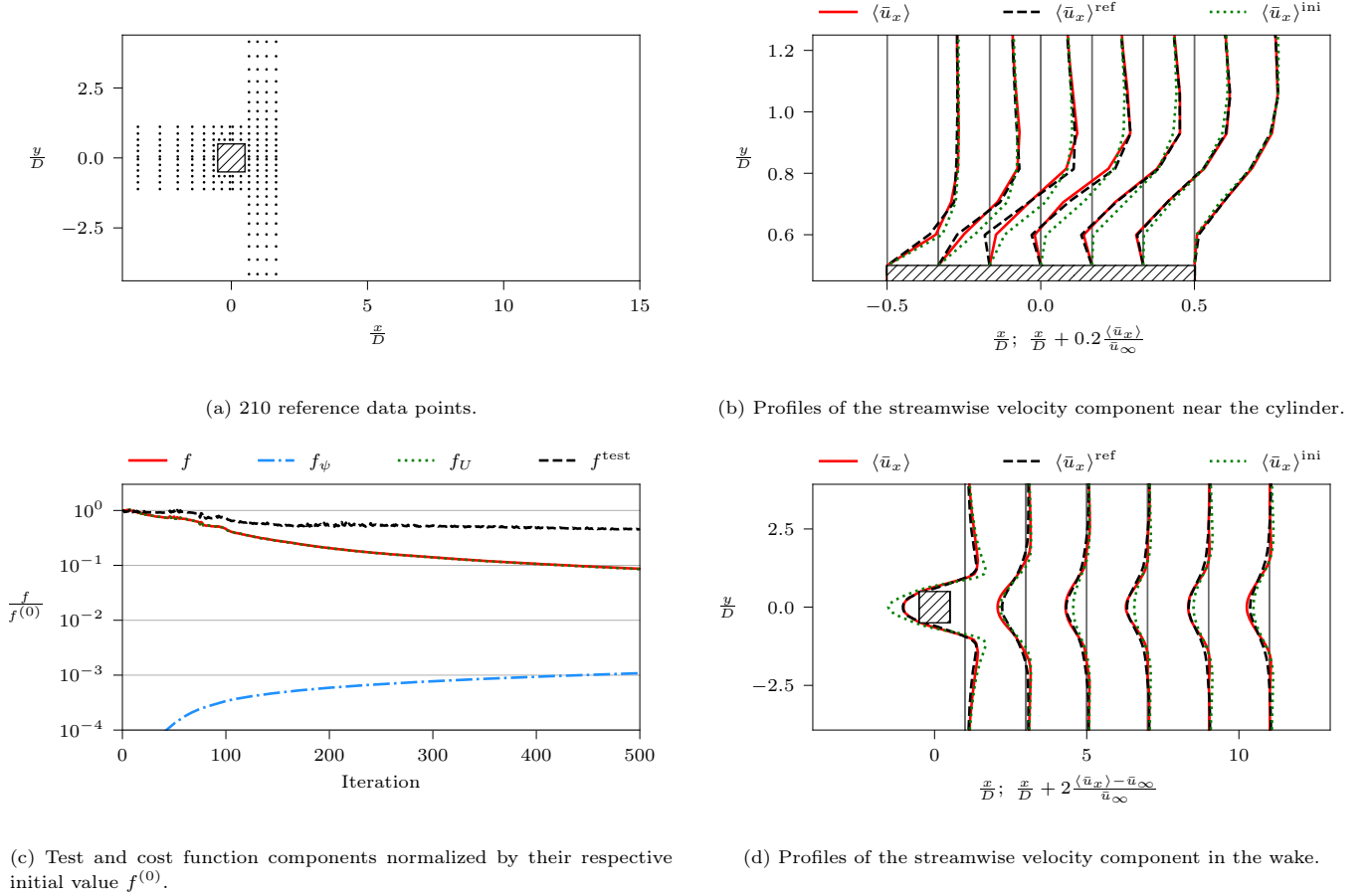
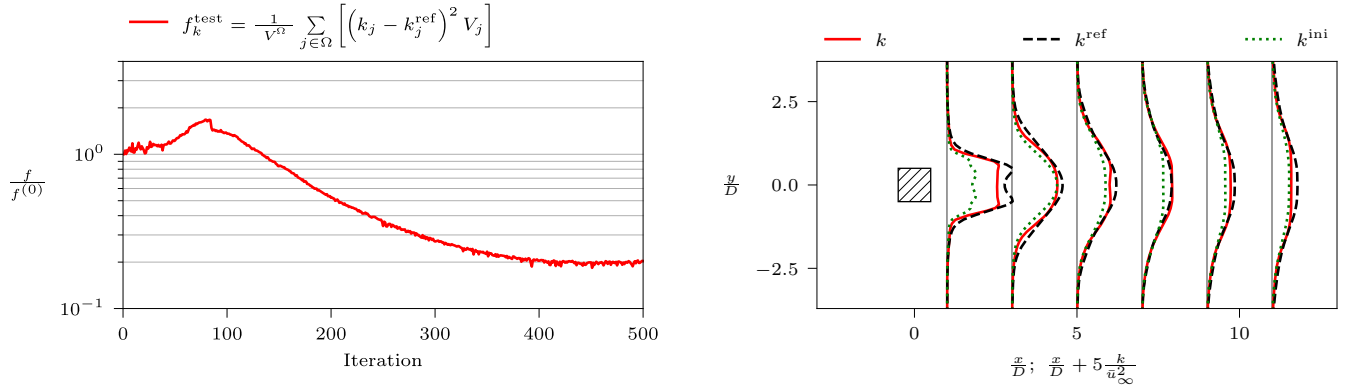


Figure 7: Optimization of the time- and spanwise-averaged flow around a square cylinder. Optimization step size is $\eta = 1 \times 10^{-1}$ with a maximum number of optimization steps $N_{\text{opt}} = 500$. The forward problem solver ran until the convergence criterion $C_U = 1$ was reached, and the regularization weight parameter was set to $C^{\text{reg}} = 1 \times 10^{-6}$.

Owing to the regularization, the averaged velocity profiles are smooth, and improvements can be observed not only around the cylinder (cf. fig. 7b) but also in its wake, as illustrated in fig. 7d. Compared to DA with a URANS model, as presented in [32], mean flow predictions also improved downstream of the cylinder, even though data was only assimilated close to the cylinder. As URANS simulations based on an eddy-viscosity model are often too dissipative, the DA using only near-cylinder reference data is not significantly improving the mean flow further downstream [32]. In contrast, LES has the advantage that large-scale motions are resolved and that only small-scale structures have to be modeled; thus, they are less dissipative. Consequently, if the objective is to improve mean flow predictions in the wake region, while observations are only available near the cylinder, it is advantageous to consider DA with LES than with URANS.

Since LES is unsteady, the corrective forcing term, even though it is stationary, has an impact on the flow dynamics. One essential dynamic feature of flow around a cylinder is the vortex shedding frequency. Therefore, the Strouhal number provides a good measure to assess whether the assimilation of averaged velocity data can improve the flow dynamics. We analyzed the uniformly sampled lift coefficient for roughly 65 vortex shedding cycles to obtain the Strouhal number. For the initial LES, the Strouhal number is $St^{\text{ini}} = 0.135$, while Trias et al. [36] report $St^{\text{ref}} = 0.132$ for the DNS reference simulation. After data assimilation, the optimized flow features a Strouhal number of $St^{\text{opt}} = 0.132$. Thus, while the initial LES is already close to the reference, assimilation of the averaged velocity reference data led to further improvement of the vortex shedding frequency, that is, to an almost perfect match with the reference.

This behavior is also reported in [32] for URANS simulations, where after optimization, however, the match with the reference Strouhal number was not perfect.



(a) TKE test function normalized with its initial value $f^{(0)}$.

(b) Profiles of the TKE in the cylinder wake.

Figure 8: Optimization of the total (resolved plus residual) TKE around a square cylinder.

Finally, the TKE is analyzed. For that purpose, profiles of the TKE are shown in the wake of the cylinder. A significant improvement can be observed, particularly in the near wake region where the TKE is highly underpredicted by the initial LES. For visualization purposes, a test function for the TKE, f_k^{test} , is introduced, analogously to the formulation in eq. (29), but for the TKE. This function is evaluated in every grid cell of the domain. As illustrated in fig. 8a, the predictions of the TKE exhibit a general improvement throughout the entire computational domain as the value of f_k^{test} decreases.

4. Conclusions and outlook

Turbulent dispersion is a crucial phenomenon in fluid dynamics where the chaotic motion leads to enhanced mixing and transport of substances, such as pollutant, or heat. Since most URANS simulations rely on eddy-viscosity models, which are often too dissipative, they lack the ability to accurately predict turbulent dispersion. LES, on the other hand, resolves some of the turbulent scales and is thus more predictive.

In this work, we proposed a three-dimensional variational assimilation of sparse time-averaged velocity reference data into LES by means of a stationary divergence-free forcing term in the respective momentum equation. The stationary discrete adjoint method was leveraged to compute the cost function gradient at a low computational cost. To do so, the filtered Navier–Stokes equations were time-averaged and subsequently used to construct a stationary adjoint equation. Making use of our efficient semi-analytical approach to compute the cost function gradient and the gradient-based optimizer for the parameter update, we demonstrated that for highly under-resolved LES, mean velocity can significantly be improved. In particular, we investigated two types of flows, namely, the flow over periodic hills with a broadband frequency spectrum and the flow around a square cylinder with periodic vortex shedding. We also demonstrated that the TKE predictions improved after the assimilation of sparse time-averaged velocity reference data for both flow configurations.

Furthermore, the stationary corrective forcing in the instantaneous LES equations improved the simulated flow dynamics. After optimization, the Strouhal number, which characterizes the periodic vortex shedding frequency, is in perfect agreement with the Strouhal number from the high-fidelity DNS.

In future work, the placement of reference data points should be investigated with the objective of reducing the number of necessary observations while ensuring optimal mean flow reconstruction, dynamic flow control, and enhanced TKE prediction. Additionally, the resolution of the computational mesh should be further studied to assess its influence on the DA procedure.

Acknowledgments

The authors would like to thank Panayotis Dimopoulos Eggenschwiler for the helpful discussions.

Appendix A. Averaging convergence criterion

We introduce a global measure for the change of an averaged field, e. g., of the velocity between time steps $(i - 1)$ and (i) as

$$C_U = \int_{\Omega} \frac{\delta \|\langle \bar{u} \rangle\|}{\delta t} dV = \int_{\Omega} \frac{\|\langle \bar{u} \rangle^{(i)} - \langle \bar{u} \rangle^{(i-1)}\|}{\Delta t^{(i)}} dV \approx \sum_k \frac{\|\langle \bar{u} \rangle_k^{(i)} - \langle \bar{u} \rangle_k^{(i-1)}\|}{\Delta t^{(i)}} V_k \quad (\text{A.1})$$

with the average velocity vector $\langle \bar{u} \rangle_k$ in cell k , the vector norm $\|\cdot\|$, the time step size Δt , and the cell volume size V_k .

References

- [1] D. C. Wilcox, *Turbulence modeling for CFD*, DCW Industries, 2006.
- [2] P. A. Durbin, Separated flow computations with the $k\text{-}\epsilon\text{-}v2$ model, *AIAA Journal* 33 (4) (1995) 659–664. doi:10.2514/3.12628.
- [3] J. Plogmann, C. Stauffer, P. Dimopoulos Eggenschwiler, P. Jenny, URANS Simulations of Vehicle Exhaust Plumes with Insight on Remote Emission Sensing, *Atmosphere* 14 (3) (2023) 558. doi:10.3390/atmos14030558.
- [4] Y. Huang, E. C. Y. Ng, N. C. Surawski, Y.-S. Yam, W.-C. Mok, C.-H. Liu, J. L. Zhou, B. Organ, E. F. C. Chan, Large eddy simulation of vehicle emissions dispersion: implications for on-road remote sensing measurements, *Environmental Pollution* 259 (2020) 113974. doi:10.1016/j.envpol.2020.113974.
- [5] E. Aristodemou, R. Arcucci, L. Mottet, A. Robins, C. Pain, Y.-K. Guo, Enhancing CFD-LES air pollution prediction accuracy using data assimilation, *Building and Environment* 165 (2019) 106383. doi:10.1016/j.buildenv.2019.106383.
- [6] D. R. Chapman, Computational aerodynamics development and outlook, *AIAA Journal* 17 (12) (1979) 1293–1313. doi:10.2514/3.61311.
- [7] U. Piomelli, E. Balaras, Wall-layer models for large-eddy simulations, *Annual Review of Fluid Mechanics* 34 (2002) 349–374. doi:10.1146/annurev.fluid.34.082901.144919.
- [8] J. H. Ferziger, M. Perić, R. L. Street, *Computational Methods for Fluid Dynamics*, Springer International Publishing, Cham, 2020. doi:10.1007/978-3-319-99693-6.
- [9] S. B. Pope, *Turbulent flows*, Cambridge University Press, 2000. doi:10.1017/cbo9780511840531.
- [10] J. Fröhlich, D. von Terzi, Hybrid LES/RANS methods for the simulation of turbulent flows, *Progress in Aerospace Sciences* 44 (5) (2008) 349–377. doi:10.1016/j.paerosci.2008.05.001.
- [11] H. Xiao, P. Jenny, A consistent dual-mesh framework for hybrid LES/RANS modeling, *Journal of Computational Physics* 231 (4) (2012) 1848–1865. doi:10.1016/j.jcp.2011.11.009.
- [12] P. R. Spalart, W.-H. Jou, M. Strelets, S. R. Allmaras, C. Liu, Z. Liu, L. Sakell, Comments on the feasibility of LES for wings and on the hybrid RANS/LES approach, in: *Proceedings of the First AFOSR International Conference on DNS/LES, 1997, 1997*, pp. 137–147.
- [13] K. Duraisamy, G. Iaccarino, H. Xiao, Turbulence modeling in the age of data, *Annual Review of Fluid Mechanics* 51 (1) (2019) 357–377. doi:10.1146/annurev-fluid-010518-040547.
- [14] A. P. Singh, K. Duraisamy, Using field inversion to quantify functional errors in turbulence closures, *Physics of Fluids* 28 (4) (Apr. 2016). doi:10.1063/1.4947045.
- [15] G. Evensen, The Ensemble Kalman Filter: theoretical formulation and practical implementation, *Ocean Dynamics* 53 (4) (2003) 343–367. doi:10.1007/s10236-003-0036-9.
- [16] M. Asch, M. Bocquet, M. Nodet, *Data assimilation: methods, algorithms, and applications*, Society for Industrial and Applied Mathematics, 2016. doi:10.1137/1.9781611974546.
- [17] G. Evensen, F. C. Vossepoel, P. J. Van Leeuwen, *Data Assimilation Fundamentals: A Unified Formulation of the State and Parameter Estimation Problem*, Springer Textbooks in Earth Sciences, Geography and Environment, Springer International Publishing, 2022. doi:10.1007/978-3-030-96709-3.
- [18] M. Meldi, A. Poux, A reduced order model based on Kalman filtering for sequential data assimilation of turbulent flows, *Journal of Computational Physics* 347 (2017) 207–234. doi:10.1016/j.jcp.2017.06.042.
- [19] X.-L. Zhang, H. Xiao, X. Luo, G. He, Ensemble Kalman method for learning turbulence models from indirect observation data, *Journal of Fluid Mechanics* 949 (Sep. 2022). doi:10.1017/jfm.2022.744.
- [20] P. Chandramouli, E. Memin, D. Heitz, 4D large scale variational data assimilation of a turbulent flow with a dynamics error model, *Journal of Computational Physics* 412 (2020) 109446. doi:10.1016/j.jcp.2020.109446.

- [21] C. He, X. Zeng, P. Wang, X. Wen, Y. Liu, Four-dimensional variational data assimilation of a turbulent jet for super-temporal-resolution reconstruction, *Journal of Fluid Mechanics* 978 (Jan. 2024). doi:10.1017/jfm.2023.972.
- [22] S. Li, C. He, Y. Liu, Unsteady flow enhancement on an airfoil using sliding window weak-constraint four-dimensional variational data assimilation, *Physics of Fluids* 35 (6) (Jun. 2023). doi:10.1063/5.0152348.
- [23] D. P. G. Foures, N. Dovetta, D. Sipp, P. J. Schmid, A data-assimilation method for Reynolds-averaged Navier–Stokes-driven mean flow reconstruction, *Journal of Fluid Mechanics* 759 (2014) 404–431. doi:10.1017/jfm.2014.566.
- [24] O. Brenner, P. Piroozmand, P. Jenny, Efficient assimilation of sparse data into RANS-based turbulent flow simulations using a discrete adjoint method, *Journal of Computational Physics* 471 (2022) 111667. doi:10.1016/j.jcp.2022.111667.
- [25] O. Brenner, J. Plogmann, P. Piroozmand, P. Jenny, A variational data assimilation approach for sparse velocity reference data in coarse RANS simulations through a corrective forcing term, *Computer Methods in Applied Mechanics and Engineering* 427 (2024) 117026. doi:10.1016/j.cma.2024.117026.
- [26] S. Li, C. He, Y. Liu, A data assimilation model for wall pressure-driven mean flow reconstruction, *Physics of Fluids* 34 (1) (Jan. 2022). doi:10.1063/5.0076754.
- [27] Y. Patel, V. Mons, O. Marquet, G. Rigas, Turbulence model augmented physics-informed neural networks for mean-flow reconstruction, *Physical Review Fluids* 9 (3) (2024) 034605. doi:10.1103/PhysRevFluids.9.034605.
- [28] S. Symon, N. Dovetta, B. J. McKeon, D. Sipp, P. J. Schmid, Data assimilation of mean velocity from 2D PIV measurements of flow over an idealized airfoil, *Experiments in Fluids* 58 (5) (Apr. 2017). doi:10.1007/s00348-017-2336-8.
- [29] L. Franceschini, D. Sipp, O. Marquet, Mean-flow data assimilation based on minimal correction of turbulence models: Application to turbulent high Reynolds number backward-facing step, *Physical Review Fluids* 5 (9) (2020) 094603. doi:10.1103/PhysRevFluids.5.094603.
- [30] S. Symon, D. Sipp, P. J. Schmid, B. J. McKeon, Mean and unsteady flow reconstruction using data-assimilation and resolvent analysis, *AIAA Journal* 58 (2) (2020) 575–588. doi:10.2514/1.j057889.
- [31] S. Ghosh, V. Mons, D. Sipp, P. J. Schmid, A robust computational framework for variational data assimilation of mean flows with sparse measurements corrupted by strong outliers, *Journal of Computational Physics* 508 (2024) 113008. doi:10.1016/j.jcp.2024.113008.
- [32] J. Plogmann, O. Brenner, P. Jenny, Variational assimilation of sparse time-averaged data for efficient adjoint-based optimization of unsteady RANS simulations, *Computer Methods in Applied Mechanics and Engineering* 427 (2024) 117052. doi:10.1016/j.cma.2024.117052.
- [33] J. Plogmann, O. Brenner, P. Jenny, Spectral adjoint-based assimilation of sparse data in unsteady simulations of turbulent flows (May 2024). doi:10.48550/arXiv.2405.20160.
- [34] B. Perot, Turbulence modeling using body force potentials, *Physics of Fluids* 11 (9) (1999) 2645–2656. doi:10.1063/1.870126.
- [35] X. Gloerfelt, P. Cinnella, Large eddy simulation requirements for the flow over periodic hills, *Flow, Turbulence and Combustion* 103 (1) (2019) 55–91. doi:10.1007/s10494-018-0005-5.
- [36] F. X. Trias, A. Gorobets, A. Oliva, Turbulent flow around a square cylinder at Reynolds number 22,000: A DNS study, *Computers & Fluids* 123 (2015) 87–98. doi:10.1016/j.compfluid.2015.09.013.
- [37] OpenFOAM v1912 (2019).
URL <https://openfoam.com>
- [38] foam-extend-5.0 (2022).
URL <https://sourceforge.net/projects/foam-extend/>
- [39] A. Yoshizawa, K. Horiuti, A statistically-derived subgrid-scale kinetic energy model for the large-eddy simulation of turbulent flows, *Journal of the Physical Society of Japan* 54 (8) (1985) 2834–2839. doi:10.1143/jpsj.54.2834.